Progress In Electromagnetics Research B, Vol. 81, 141–162, 2018

Electromagnetic Scattering and Emission by Ocean Surfaces Based on Neighborhood Impedance Boundary Condition (NIBC) with Dense Grid: Accurate Emissivity and Sensitivity to Salinity

Tai Qiao[1], Yanlei Du[1, 2], and Leung Tsang[1, *]

Abstract—In order to have the required accuracies in method of moments (MoM) for numerical simulations of ocean scattering at microwave frequencies, we need to account for the much larger wavenumber of sea water relative to that of air. This paper presents simulation results of 2D ocean surface scattering with the required accuracies and that energy conservation is obeyed to 0.01%. A dense grid is required to discretize the MoM dual surface integral equation with up to 240 surface unknowns (120 surface electric field unknowns and 120 surface magnetic field unknowns) per free space wavelength. To solve the matrix equation efficiently, we develop a neighborhood impedance boundary condition (NIBC) technique to solve the matrix equation. We next calculate the emissivities of ocean surfaces using NIBC on surface integral equations using pulse basis/point matching and the Nystrom method. Results are illustrated for L-band and show that emissivities using NIBC combined with Nystrom are accurate to 2×10^{-4} for vertical polarization and 10^{-4} for the horizontal polarization. This means that the new method can meet the accuracy goal of 0.2 psu salinity retrieval for the NASA Aquarius mission. Results of surface fields and emissivities are also compared to that of impedance boundary condition (IBC) which requires only 10 unknowns per free space wavelength.

1. INTRODUCTION

The studies of electromagnetic scattering and emission by ocean surfaces are important for remote sensing of ocean dynamic parameters, e.g., sea surface wind (SSW) and sea surface salinity (SSS) [1]. For ocean scattering, analytical methods include the small perturbation method (SPM), first and second order (SPM2) [2–6], the advanced integral equation model (AIEM) [7], the small slope approximation (SSA) [8–12] and the two scale model (TSM) [13–15]. The challenges are to obtain accurate results. These are particular difficult for cross polarization which are much smaller than co-polarization. The other difficult case is the study of emissivity which has only small changes due to small changes of salinity. For the Aquarius mission [16–19], the accuracy requirement of measuring salinity is 0.2 psu (practical salinity unit) which requires that the emissivity to be within 4.9×10^{-4} for vertical polarization and 3.4×10^{-4} for horizontal polarization.

With the advances of computers and computational electromagnetics, ocean scattering and emission have been studied with numerical solutions of Maxwell equations [20–25]. The surface integral equations with Method of Moments (MoM) solution is the most common method [26]. However, accuracy issue is a major concern for numerical methods particularly for the convergence of emissivity with surface samplings in MoM implementation. The accuracies of emissivities are related to energy conservation requirement in numerical simulations. Prior simulations of ocean scattering, based on MoM, satisfy energy conservation to within 0.5% at best. For ocean surfaces, sea water with a salinity of 35 psu at a

Received 7 May 2018, Accepted 25 June 2018, Scheduled 9 July 2018

* Corresponding author: Leung Tsang (leutsang@umich.edu).

[1] Radiation Laboratory, Department of Electrical Engineering and Computer Science, The University of Michigan, Ann Arbor, MI 48109-2122, USA. [2] State Key Laboratory of Remote Sensing Science, Institute of Remote Sensing and Digital Earth, Chinese Academy of Sciences, Beijing 100101, China.

water temperature of 10°C at L band has a relative permittivity of $75+61i$ with corresponding complex refractive index $9.26+3.29i$.

In such cases of large ocean wavenumber relative to air for the dual surface integral equations, there are two Green's functions g and g_1 with respective wave numbers of k and k_1 where k is the air wavenumber, and k_1 is the sea water wavenumber. The dual surface integral equations are computational expensive because: (i) The number of unknowns is twice that of a single surface integral equation using only g. (ii) The discretization of surface based on g_1 has to be much denser than that of g. The usual discretization of g, the air Green's function, is 10 points per wavelength λ. The interval of discretization Δx is 1/10 of a wavelength. Because k_1 for ocean surface is 9.3 times larger, the discretization of the surface should be 93 points per wavelength [27]. Thus the number of unknowns for the dual surface integral equations is many time larger than that of the perfect electric conductor (PEC) or impedance boundary condition (IBC) approach. This increase is even more serious for 3D problems. In addition, it is found that the condition number with such a dense grid and large number of unknowns is much higher creating convergence issues for an iterative solver. Thus surface discretization with more than 32 points per free space wavelength has not been used before.

In the past, researchers in ocean scattering have adopted two simplifying approaches. The first approach is assuming that the ocean is a perfect electric conductor (PEC) with tangential electric field equal to zero [20]. This gives a single surface integral equation with only g. Thus for a 100 wavelengths surface, the total number of unknowns is only 1000. This approach ignores the finite value of the relative permittivity of ocean. In the second approach, known as impedance boundary condition (IBC) [22, 23] states that the tangential electric field of the surface is equal to the wave impedance of the dielectric medium times the tangential magnetic field. This approximation is exact for a flat surface and may be valid when the radius of curvature of the surface at a point is much larger than the wavelength. The approach also requires only a single surface integral equation with 10 points per wavelength. For a 100 wavelength surface, the number of unknowns for IBC is also 1000.

In this paper, we address the accuracy issue by using the dual surface integral equations. We use two methods: (i) the pulse basis function with point matching of dense grid with up to 120 points per wavelength, so that $\Delta x = \lambda/120$ and (ii) using Nystrom method with 5th order basis function, with the same number of surface field unknowns as (i). Both (i) and (ii) are using the same surface profile but simulation is conducted under fair comparison so that (i) and (ii) have the same number unknowns. To accelerate the computations, we use a novel method that takes advantage that the sea surface is heavily attenuative so that using the wavenumber k_1 gives the fast decaying property of Green's function in lower medium along with the propagating distance. This means that if one excite one point on the surface, only nearby points are being influenced due to the fast decaying property of waves in a lossy medium. In 2D problem, this means the impedance matrix is a banded matrix for the lower medium integral equation. The band nature relating fields to each other is utilized and is further found to lead to a much smaller conditioner number and a fast convergence. This new method exploits the band nature of Green's function and formulates the correct relationship of surface tangential electric field and tangential magnetic fields. We name this method the Neighborhood Impedance Boundary Condition (NIBC). There is a significant difference between the proposed NIBC and existed fast methods, for instance, Physics-Based Two-Grid (PBTG) Method [28]. PBTG solves the dual surface integral equations directly. As discussed in the paper, solving the dual surface integral equations directly has poor conditioner number that becomes worse when the number of points are increased to 64 points per wavelength. NIBC first solves the lower equation with the Green's function of sea water. Then the solution is substituted into the air equation. That gives much lower conditioner number even when the number of points is increased to 120 points per wavelength as shown in this paper. The compliance of energy conservation is achieved first time with NIBC. This is analogous to SPM2 which has been shown to obey energy conservation [5, 6].

The organization of this paper is as follows. In Section 2, the surface integral equations are discussed with the number of points and the number of unknowns. The ocean profiles used in the numerical simulations are also described. Section 3 describes the proposed NIBC method. In Section 4, the surface fields of various methods are compared. In Section 5, comparisons of emissivity are made showing the accuracies. The sensitivities to salinity are also shown. The Nystrom method is described in Appendix A.

2. SURFACE INTEGRAL EQUATIONS

In this section, we describe the formulations used in Dual SIE and IBC. Also tapered wave incidence and the ocean profiles used in the numerical simulations are described in this section.

2.1. Dual Surface Integral Equations

For the 2D rough surface scattering problem, the governing Dual surface integral equations (SIE) derived from extinction theorem from both air and medium are [26]

$$-\int dx' \left[\psi\left(x'\right)\sqrt{1+\left(f'\left(x'\right)\right)^2}\frac{\partial}{\partial n'}g\left(x,z;x',z'\right)-g\left(x,z;x',z'\right)u\left(x'\right)\right]_{z'=f(x')}=\psi_{inc}\left(x,z\right) \quad (1)$$

$$-\int dx' \left[\psi\left(x'\right)\sqrt{1+\left(f'\left(x'\right)\right)^2}\frac{\partial}{\partial n'}g_1\left(x,z;x',z'\right)-g_1\left(x,z;x',z'\right)\frac{1}{\rho}u\left(x'\right)\right]_{z'=f(x')}=0 \quad (2)$$

$$u\left(x'\right)=\sqrt{1+\left(f'\left(x'\right)\right)^2}\frac{\partial}{\partial n'}\psi\left(x'\right) \quad (3)$$

where $g(x,z;x',z')$ is the Green's function in the air which is $\frac{i}{4}H_0^{(1)}(k\sqrt{(x-x')^2+(z-z')^2})$. $g_1(x,z;x',z')$ is the Green's function in the medium which is $\frac{i}{4}H_0^{(1)}(k_1\sqrt{(x-x')^2+(z-z')^2})$. Here, k and k_1 are the wavenumbers in the air and lower medium, respectively, which are defined as

$$\begin{aligned} k&=\omega\sqrt{\mu\varepsilon}\\ k_1&=\omega\sqrt{\mu_1\varepsilon_1}\end{aligned} \quad (4)$$

where ω is the angular frequency of incident wave. μ, ε and μ_1, ε_1 are the permeability and permittivity of the air and the lower medium, respectively.

Other parameters shown in Dual SIE are defined as follows: ψ is the electric field if it is TE polarization and is magnetic field if it is TM polarization. u is proportional to magnetic field for TE case and is proportional to electric field for TM case. $z=f(x)$ is the rough ocean surface profile and $f'(x)$ is the slope of the surface. $\hat{n}$ is the normal vector of the surface. ρ is an indicator of TE and TM incidence which is $\frac{\mu}{\mu_1}$ for TE case and $\frac{\varepsilon}{\varepsilon_1}$ for TM case. ψ_{inc} is the incidence wave.

Based on the method of moment (MoM), we perform point matching to the surface integral Equations (1) and (2), and get

$$\sum_{n=1}^{N}A_{mn}u_n+\sum_{n=1}^{N}B_{mn}\psi_n=\psi_{inc}\left(x_m,f\left(x_m\right)\right) \quad (5)$$

$$\frac{1}{\rho}\sum_{n=1}^{N}A_{mn}^{(1)}u_n+\sum_{n=1}^{N}B_{mn}^{(1)}\psi_n=0 \quad (6)$$

For matrix elements in Equation (5), we have

$$A_{mn}=g\left(x_m,z_m;x_n,z_n\right)\Delta x \quad \text{for } m\neq n \quad (7)$$

$$A_{mm}=\frac{i}{4}\Delta x\left[1+i\frac{2}{\pi}\ln\left(\frac{\gamma k\Delta x}{4e}\sqrt{1+\left(f'\left(x_m\right)\right)^2}\right)\right] \quad (8)$$

$$B_{mn}=-\Delta x\sqrt{1+\left(f'\left(x_n\right)\right)^2}\left[\frac{\partial}{\partial n'}g\left(x_m,z_m;x_n,z_n\right)\right] \quad \text{for } m\neq n \quad (9)$$

$$B_{mm}=\frac{1}{2} \quad (10)$$

For matrix elements in Equation (6), we have

$$A_{mn}^{(1)}=g_1\left(x_m,z_m;x_n,z_n\right)\Delta x \quad \text{for } m\neq n \quad (11)$$

$$A_{mm}^{(1)} = \frac{i}{4}\Delta x\left[1+i\frac{2}{\pi}\ln\left(\frac{\gamma k_1 \Delta x}{4e}\sqrt{1+\left(f'\left(x_m\right)\right)^2}\right)\right] \tag{12}$$

$$B_{mn}^{(1)} = -\Delta x\sqrt{1+\left(f'\left(x_n\right)\right)^2}\left[\frac{\partial}{\partial n'}g_1\left(x_m,z_m;x_n,z_n\right)\right] \quad \text{for } m\neq n \tag{13}$$

$$B_{mm}^{(1)} = -\frac{1}{2} \tag{14}$$

For the sake of simplicity, we can express Equations (5) and (6) in matrix notations as

$$\left[\begin{array}{cc} \overline{\overline{A}} & \overline{\overline{B}} \\ \frac{1}{\rho}\cdot\overline{\overline{A}}_1 & \overline{\overline{B}}_1 \end{array}\right]\left[\begin{array}{c} \overline{u} \\ \overline{\psi} \end{array}\right] = \left[\begin{array}{c} \overline{\psi}_{inc} \\ \overline{0} \end{array}\right] \tag{15}$$

2.2. Impedance Boundary Condition

In above surface integral equations, for usual perfect electric conductor (PEC) scattering problem, discretization of surface with 10 points per free space wavelength is usually enough to get correct results. However, for dielectric medium with a large permittivity, 10 points per wavelength is far from enough. A usual criterion is to discretize the gird so that there are around 10 points per medium wavelength. This will dramatically increase the number of unknowns. To avoid this, impedance boundary condition (IBC) has been introduced in the SIE [22].

The IBC is based on the assumption that the surface electric field and surface magnetic field is related through the following relationship

$$\bar{E}|_{\tan} = \eta_1 \cdot \widehat{n}\times\bar{H} \tag{16}$$

where $\bar{E}|_{\tan}$ is tangential electric field and η_1 is the impedance of the lower medium.

For the 2D problem, based on Equation (16), we can derive

$$\frac{1}{i\omega\varepsilon}\left(\widehat{n}\cdot\nabla\psi\left(x\right)\right) = -\eta_1\psi\left(x\right) \quad \text{for TM polarization} \tag{17}$$

$$\frac{1}{i\omega\mu}\left(\widehat{n}\cdot\nabla\psi\left(x\right)\right) = -\frac{1}{\eta_1}\psi\left(x\right) \quad \text{for TE polarization} \tag{18}$$

Combining Equations (17), (18) and (3), we have

$$u\left(x'\right) = \sqrt{1+\left(f'\left(x'\right)\right)^2}\left[-ikr_a\psi\left(x'\right)\right] \tag{19}$$

where

$$\begin{aligned} r_a &= -\frac{\eta_1}{\eta} \quad \text{for TM polarization} \\ r_a &= -\frac{\eta}{\eta_1} \quad \text{for TE polarization} \end{aligned} \tag{20}$$

Thus for either TM or TE polarization we can substitute Equation (19) into Equation (1) to get a simplified equation which only has either electric fields or magnetic fields as the unknowns.

2.3. Tapered Incidence Wave

In numerical simulations based on SIE, the infinite rough surface has to be truncated to a finite length of L. Thus, to avoid the artificial edge reflections created by the truncation, a tapered incident wave is used in our simulations which is defined as [26]

$$\psi_{inc}\left(x,z\right) = \exp\left(ik\left(x\sin\theta_i - z\cos\theta_i\right)\left(1+w\right)\right)\exp\left(-\frac{\left(x+z\tan\theta_i\right)^2}{g^2}\right)^2 \tag{21}$$

where $\psi_{inc}(x,z)$ is the incident field which is the function of position (x,z). θ_i is the wave incident angle. g is the tapering parameter which is often chosen as $L/4$, where L is the length of surface. The w function is introduced so that ψ_{inc} obeys wave equation which is defined as

$$w = \frac{2\dfrac{(x + z\tan\theta_i)^2}{g^2} - 1}{(kg\cos\theta_i)^2} \tag{22}$$

2.4. Surface Profiles and Point's Number Discussion

In our studies, besides the IBC, we also use method of moment (MoM) with different basis functions to solve the SIE. We take two approaches based on MoM. The first approach uses the pulse basis function with point matching with up to 120 points per wavelength. The second approach is based on Nystrom method with 5th order basis function [29, 30]. The details of Nystrom method are described in Appendix A. Since we are about to address the accuracy issue of rough ocean surface scattering and emission with these methods, the impact of surface sampling on accuracy needs to be studied. For a fair comparison, the number of surface field unknowns of different methods will be same.

For the ocean surface profiles used in the numerical simulations, the Elfouhaily's unified ocean wave spectrum is used [31]. Figure 1 shows the ocean surface profiles for different methods with different samplings. The sparse sampling surfaces are obtained from the denser surface by resampling. The surface length of simulation is 60 times of L-band (1.26 GHz) incident wavelength. Surface wind speed is chosen as 5 m/s. This surface profile is used for all cases except otherwise indicated. In Table 1, the numbers of unknowns of different samplings for different methods on the rough surface are shown. It is noted that, for each sampling case, pulse/point matching and Nystrom have twice unknowns of that of IBC.

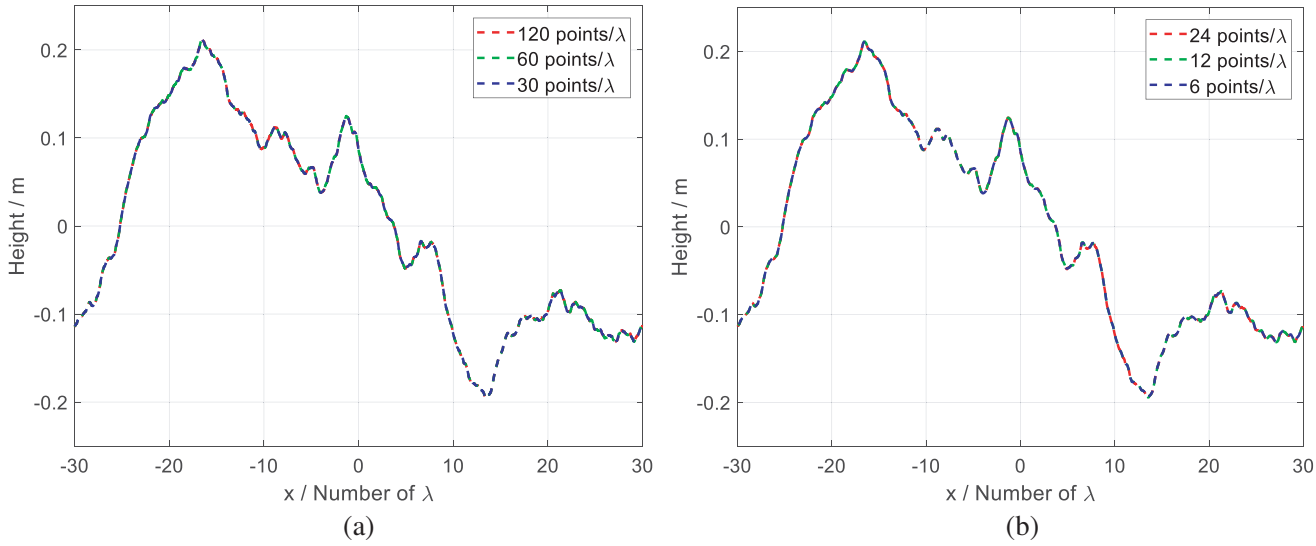

Figure 1. Ocean surface profiles with different samplings used in numerical simulations. λ is the wavelength of L-band incidence. (a) Profiles for IBC and MoM with pulse/point matching. (b) Profiles for MoM with Nystrom method.

3. NEIGHBORHOOD IMPEDANCE BOUNDARY CONDITION

3.1. Formulations of NIBC

In this section we are describing the proposed novel method, neighborhood impedance boundary condition (NIBC) [32], to accelerate the Dual SIE solving process for highly dielectric lossy surfaces [33].

Table 1. Comparison of the number of unknowns of IBC, pulse/point matching and Nystrom.

Number of Unknowns for a 60λ long surface				
Methods		IBC	pulse/point matching	Nystrom
Unknown type		either ψ or u	ψ and u	ψ and u
Δx	$\frac{\lambda}{30}$	1800	3600	3600
	$\frac{\lambda}{60}$	3600	7200	7200
	$\frac{\lambda}{120}$	7200	14400	14400

Different from usual method which solves Equation (15) directly, the proposed NIBC method is trying to solve lower equation first and then the upper one. Thus, we have

$$\overline{u} = -\overline{\overline{A}}_{1\rho}^{-1}\overline{\overline{B}}_1\overline{\psi} = \overline{\overline{M}\psi} \tag{23}$$

where $\overline{\overline{M}}$ is the matrix relating $\bar{u}$ and $\bar{\psi}$ and

$$\overline{\overline{A}}_{1\rho} = \frac{1}{\rho}\cdot\overline{\overline{A}}_1 \tag{24}$$

Then substitute Equation (23) into the upper equation in Equation (15), gives

$$\left(-\overline{\overline{A}\overline{A}}_{1\rho}^{-1}\overline{\overline{B}}_1 + \overline{\overline{B}}\right)\overline{\psi} = \overline{\psi}_{inc} \tag{25}$$

Equation (25) becomes the final equation we are solving.

As mentioned earlier, since the permittivity of sea water has a large imaginary part, the waves will decay fast with the travelling distance. Thus the matrix $\overline{\overline{A}}_1$ and $\overline{\overline{B}}_1$ are actually band matrix. Figure 2 shows a comparison of 2D Green's function of air and sea water in terms of absolute value. It is easy to see that the Green's function in the sea water decays very fast. Even for a propagating distance of one λ, the absolute value drops to 10^{-12} which is much lower than the Green's function in the air. This means that $\overline{\overline{A}}_1$ and $\overline{\overline{B}}_1$ actually behave like a band matrix. The matrix elements quickly decrease when moving away from the diagonal line. Therefore, we can set up a bandwidth (BW) of the matrices that the matrix entries outside the BW are set to be zero. This means only matrix elements within the BW are considered. Apparently, the selection of BW determines the accuracy. To test the accuracy of proposed NIBC, the brute force solution to Equation (25) in the manuscript is set to be the benchmark, which solves equation with the whole matrices $\overline{\overline{B}}_1$, $\overline{\overline{A}}_{1\rho}$. And we found that even a small bandwidth can give quite accurate results to meet satellite accuracy requirement.

In our numerical implementation, the BW is chosen to be $\frac{\lambda}{2}$ to meet our accuracy requirement. Now the problems reduces to solve for the inverse matrix of a diagonal matrix with a bandwidth BW. Here we propose a banded matrix solver for this matrix-inverse problem. The following is an expression of the definition of inversion.

$$\overline{\overline{A}}_1\overline{\overline{A}}_1^{-1} = \overline{\overline{I}} \tag{26}$$

According to the physical meaning of $\overline{\overline{A}}_1^{-1}$, we further found that $\overline{\overline{A}}_1^{-1}$ is also band matrix. Then in order to obtain the inverse of $\overline{\overline{A}}_1$, we can solve for each column of $\overline{\overline{A}}_1^{-1}$ one at a time. That is each time we are solving

$$\overline{\overline{A}}_1\overline{a}_n = \overline{e}_n \tag{27}$$

where $\bar{a}_n$ is the nth column of the inverse of the matrix $\overline{\overline{A}}_1$, and $\bar{e}_n$ is a column vector with all zero elements except the nth element.

Figure 3 shows an example about how we invert the matrix. In this case, the BW is 3 grids and the figure is showing a case to solve for the 4th column of the matrix $\overline{\overline{A}}_1^{-1}$. Then we just need to

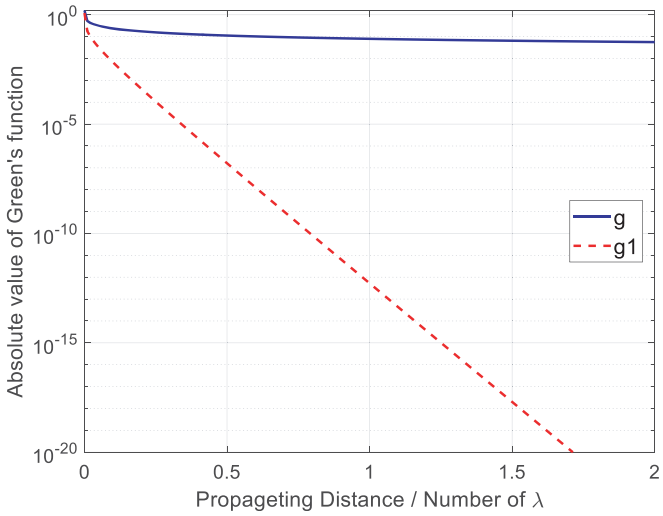

Figure 2. Comparison of 2D Green's function in the air and sea water as a function of propagating distance.

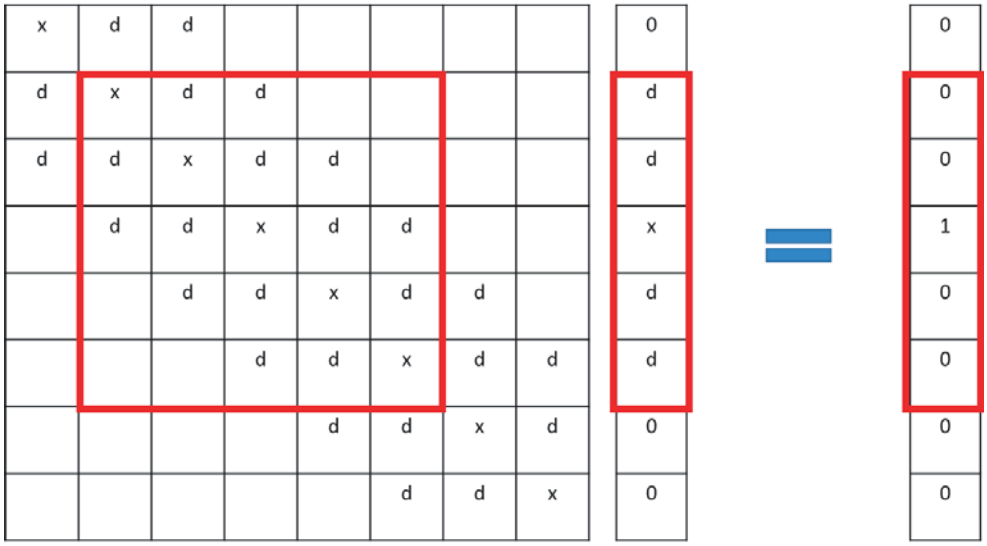

Figure 3. Fast method for band matrix inversion.

solve an inversion problem of size 5 by 5. The 'x' and 'd' in the figure represent diagonal and off-diagonal elements, respectively. Thus compared to usual method of inversing a matrix which is of the computation complexity order $O(N^3)$, our method will only require $O(N \cdot BW^3)$.

To further improve accuracy, we further use the Nystrom method for testing and basis functions. The NIBC are also used in the Nystrom method formulation. The details are described in the Appendix A.

3.2. NIBC for Alleviating Numerical Issues Brought by Dense Grid

As mentioned above, due to the much larger wavenumber in the lower SIE, a much denser discretization is required to solve the Dual SIE accurately. Besides the huge consumption of memory due to more number of unknowns, the slow convergence problems in iterations also arise. Figure 4 shows the residual error along with iterative steps produced by generalized minimal residual method (GMRES) for two kinds of surfaces: 60λ long surface with 60 points/λ and 60λ long surface with 10 points/λ for both

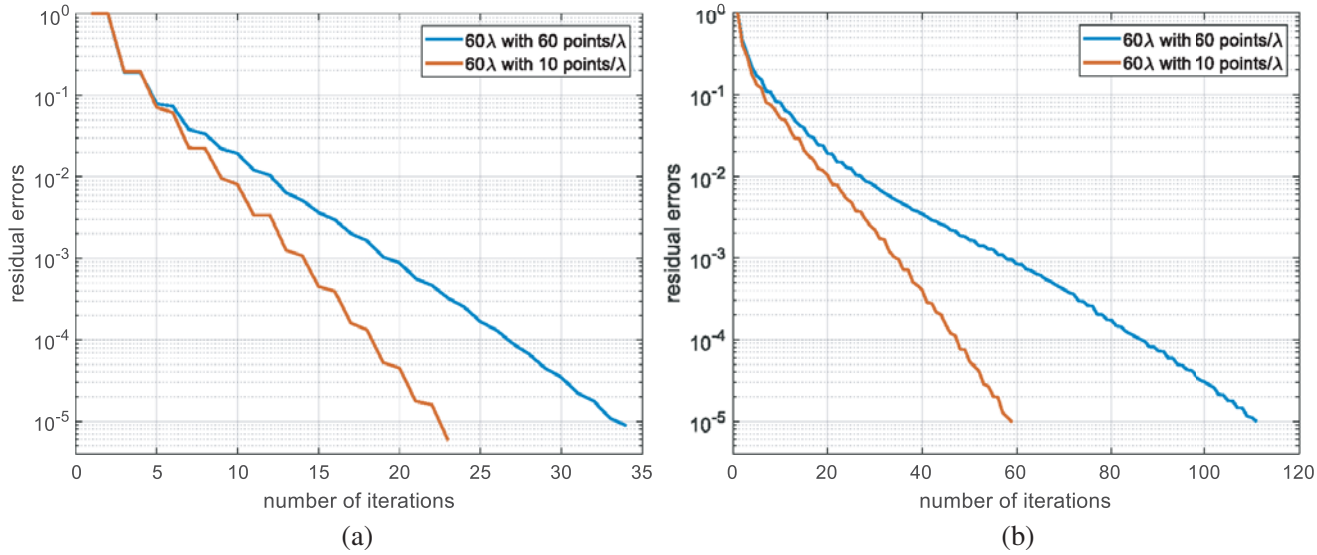

Figure 4. Residual error changing with iterations for two kinds of surfaces: 60λ long surface with 60 points/λ (blue curve) and 60 λ long surface with 10 points/λ (orange curve) for both (a) TM polarization and (b) TE polarization.

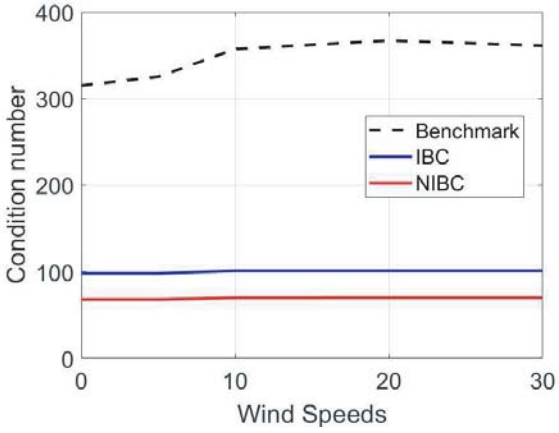

Figure 5. Condition number comparison for IBC, NIBC, and benchmark method for ocean surfaces.

TM and TE incidence. Here the λ is the wavelength of incidence. It is seen that the dense grid case converges much slower than the coarse grid case. This phenomenon has also been found in 3D problem case: the dense grid always converge much slowly than coarse grid case.

The proposed NIBC can deal with this convergence problem efficiently. In Figure 5, we plot the condition number comparison for IBC, NIBC, and benchmark method (Direct MoM) for ocean surfaces. It is seen that the NIBC has a much smaller condition number than IBC and benchmark solution. The benchmark solution is defined as the solution of solving Equation (15) directly. Thus NIBC has actually changed the property of the impedance matrix. A small condition number means a good matrix property and a fast convergence rate when using iterative solvers. A near field preconditioner was used in a previous paper [34]. However, the conditioner number is still poor for 64 points per wavelength. The energy conservation was only improved slightly.

In Table 2 we compare the CPU time for the iterations between direct MoM for solving Equation (15) and NIBC for the same cases. We can see that since the impedance matrix of NIBC has smaller condition number thus the iterations take less time to converge to a desired residual error.

Table 2. Comparison of CPU time by direct MoM and MoM/NIBC.

Surface length is 60λ			
Number of Unknowns	Direct MoM	MoM + NIBC	Δx
7200	19.9 sec	1.7 sec	$\frac{\lambda}{60}$
14400	96.7 sec	5.3 sec	$\frac{\lambda}{120}$

4. RESULTS AND DISCUSSION OF SURFACE FIELDS

In this section we compare the surface fields among various methods. The rough ocean surface profiles generated with Elfouhaily spectrum are described in Section 2.4. The relative permittivity of sea water is calculated with K-S model based on Debye equation with sea surface temperature at 20°, sea surface salinity at 35 psu and frequency at 1.26 GHz [33]. The error of using Frobenius norm is used to calculate the difference between two arrays. It is defined as

$$\text{error}\% = \frac{\|\text{array1} - \text{array2}\|_F}{\|\text{array1}\|_F} \times 100\% \tag{28}$$

where $\| \ \|_F$ is the Frobenius norm

$$\|C_{n\times 1}\|_F = \sqrt{\sum_{i=1}^{n} |c_i|^2} \tag{29}$$

4.1. Comparison of Pulse/Point Matching with Coarse and Dense Grid

Figure 6 shows the comparison of surface fields calculated by MoM pulse/point matching for both TE and TM case for different discretization density using the same surface profile. The x axis is the surface length in wavelength. The y axis is the absolute values of surface fields on the surface. As is shown in Figure 6, surface fields are closed to each other when the surface sampling densities are 30, 60, 120 points per wavelength, but they are quite different from the results with coarse grid which is 10 points per wavelength. This means that for Dual SIE, sampling density with 10 points per wavelength is far from enough to obtain accurate results. This validates our statement that dense grid is necessary for medium with a large permittivity.

To quantitatively evaluate the numerical results of MoM pulse/point matching based on Dual SIE for different discretization densities, the errors of surface fields are given in Table 3. The benchmark is chosen as numerical results with 120 points per wavelength samplings. As the table shows, compared to the quite large errors when sampling density is 10 points per wavelength, errors are relatively small when samplings are denser than 30 points per wavelength. This indicates that the numerical results begin to converge when grids are denser than 30 points per wavelength. Hence, to obtain accurate enough emissivity of ocean surface, dense grids of surface are required.

Table 3. Errors of MoM pulse/point matching calculation results with different samplings on surfaces. The benchmark is chosen as numerical results with 120 points per wavelength samplings.

Surface length is 60λ				
Δx	Error (%) of ψ		Error (%) of u	
	TM	TE	TM	TE
$\frac{\lambda}{10}$	10.56	121.5	55.91	9.951
$\frac{\lambda}{30}$	2.166	1.883	3.175	1.760
$\frac{\lambda}{60}$	1.166	0.4337	1.851	1.195
$\frac{\lambda}{120}$	benchmark	benchmark	benchmark	benchmark

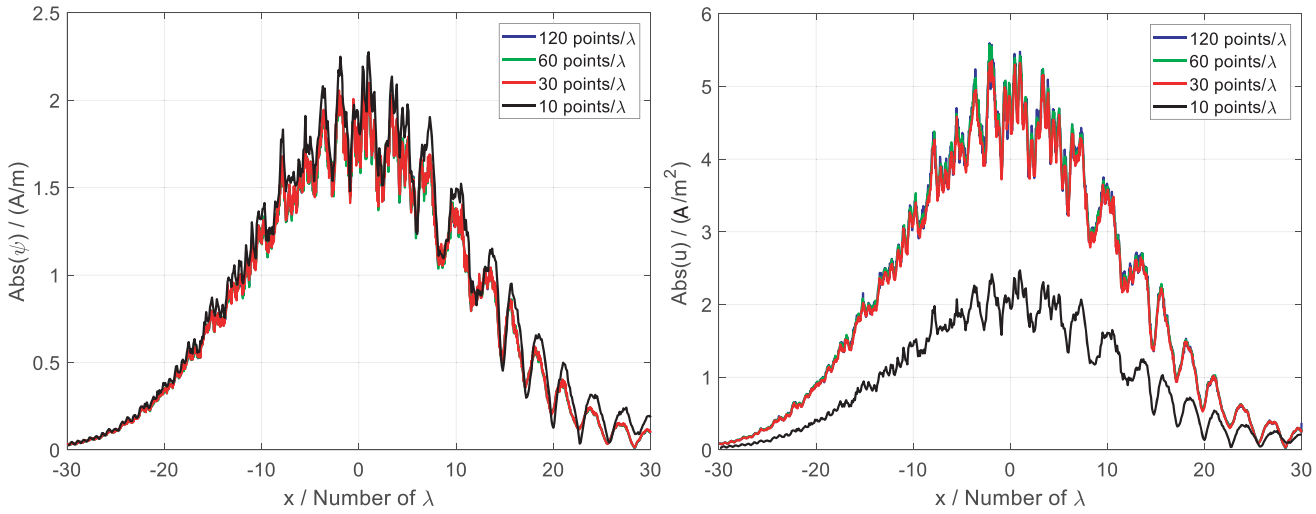

(a)

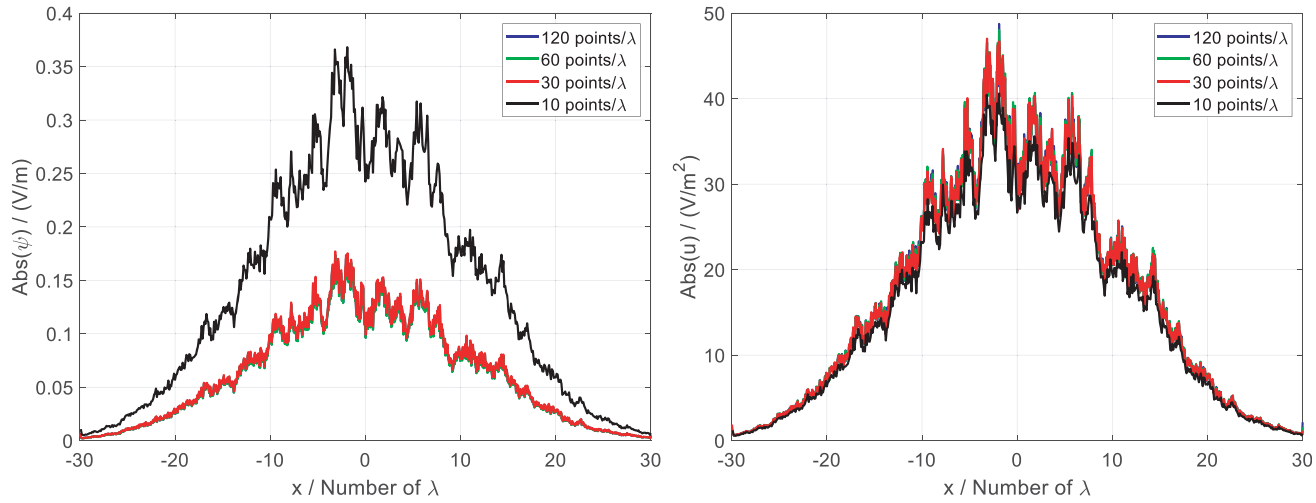

(b)

Figure 6. Comparisons of surface fields calculated by using MoM pulse/point matching based on dual SIE with different dense samplings on surfaces. (a) TM case (b) TE case; Left panels are ψ; Right panels are u.

Table 4. Errors of surface fields and currents with IBC for both TE and TM polarization. The benchmark is chosen as numerical results of Dual SIE with 120 points per wavelength samplings.

Surface length is 60λ				
Method/Δx	Error (%) of ψ		Error (%) of u	
	TM	TE	TM	TE
IBC/$\frac{\lambda}{10}$	3.782	2.347	4.287	2.628
Dual SIE/$\frac{\lambda}{120}$	benchmark	benchmark	benchmark	benchmark

4.2. Comparisons between IBC and Dual SIE

The impedance boundary condition (IBC) [22, 23] was proposed by making the approximation that the tangential electric field of the surface is equal to the wave impedance of the dielectric medium times the

tangential magnetic field. Thus it reserves only the upper equation in Dual SIE with only half unknowns, and the requirement of surface sampling is 10 points per wavelength since only green function of free space is used.

In Table 4, the errors of surface fields with IBC for both TE and TM polarization are given. The benchmark is chosen as numerical results of Dual SIE with 120 points per wavelength samplings. As shown in the table, the errors are relatively large considering the high accuracy requirement of ocean emissivity. Further accuracy analyses of IBC on emissivities are shown in the following section.

4.3. Comparisons among Direct MoM, IBC and NIBC

In Figure 7, we plot the error defined in Equation (28) of matrix $\overline{\overline{M}}$ in terms of Frobenius norm for TM polarization. $\overline{\overline{M}}$ is relating surface magnetic field and surface electric field and is defined in Equation (23). For IBC, the matrix $\overline{\overline{M}}$ is simply a diagonal matrix due to the definition of IBC as defined in Equation (19). The case is the ocean surfaces with different wind speeds. From Figure 7 we see that the error of NIBC is less than 0.1% while the error norm for IBC is more than 80%.

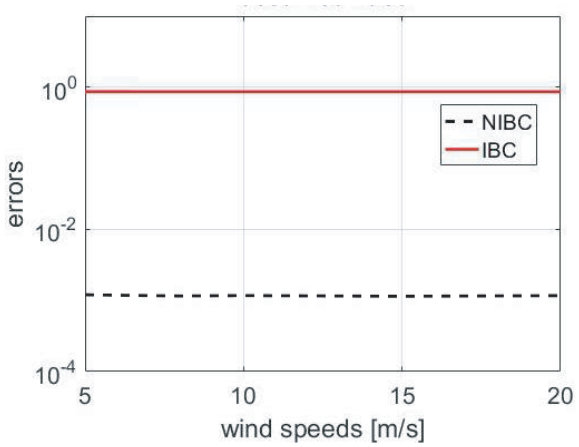

Figure 7. Comparison of matrix $\overline{\overline{M}}$ between NIBC and IBC with direct MoM for ocean surfaces under different wind speeds for TM polarization.

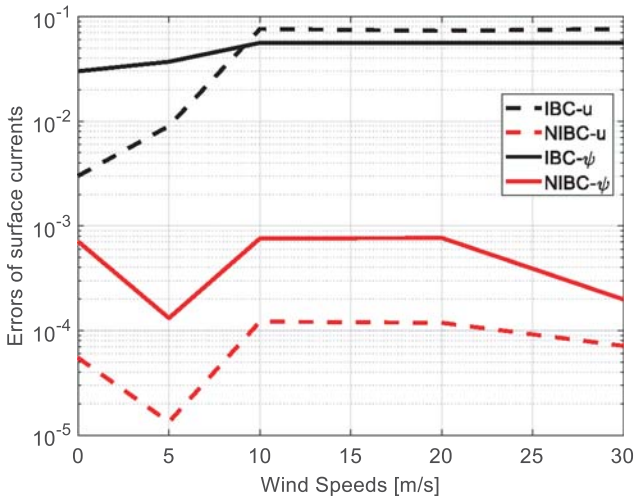

Figure 8. Surface fields errors of IBC and NIBC compared to direct MoM for ocean surface under different wind speeds for TM polarization.

Figure 8 shows the comparison of surface fields errors of IBC and NIBC compared to benchmark solutions (direct MoM) for TM polarization. The red lines are surface fields calculated by NIBC and black lines are IBC. It is also observed that the error norm of NIBC is less than 0.1% for ocean surfaces under different winds speeds while IBC has an error norm of more than 1%.

In our numerical implementations, the NIBC is also used with MoM Nystrom. Table 5 gives the errors of NIBC with pulse/point matching and Nystrom. From Table 5, it can be seen that the errors of surface by using Nystrom + NIBC are quite small. However, the errors of pulse/point matching + NIBC are relatively lager.

5. OCEAN EMISSIVITY AND SENSITIVITY TO SALINITY

5.1. Accuracies of Emissivity with Various MoM Methods

In this section, we apply the NIBC to calculate the emissivity of ocean surface. We have used the Klein and Swift [33] model to convert PSU into dielectric constants. Then we simulate the emission of sea surface using the different dielectric constant. For example, the retrieval goal of Aquarius mission is

Table 5. Errors of NIBC with pulse/point matching and Nystrom. The benchmarks are MoM pulse/point matching and MoM Nystrom, respectively.

Surface length is 60λ				
Method/Δx	Error (%) of ψ		Error (%) of u	
	TM	TE	TM	TE
Pulse/Point matching + NIBC/$\frac{\lambda}{120}$	6.828×10^{-2}	1.553	4.536	2.339
Nystrom + NIBC/$\frac{\lambda}{120}$	7.200×10^{-6}	3.475×10^{-5}	3.966×10^{-5}	1.166×10^{-5}

0.2 PSU. Then we studied the emission of sea surface under two PSUs: 34 and 34.2. We can get two dielectric constants for 34 and 34.2 psu respectively. Then we obtain the emission accuracies for both TE and TM incidence. The computed results from the numerical method are the surface electric fields (magnetic currents) and surface magnetic fields (electric currents). Through these two surface fields, we compute the power absorbed by the lossy medium (absorption) and power scattered outside (reflected power). The energy conservation is defined as follows:

$$\text{energy conservation} = \frac{\text{absorption + reflectivity}}{\text{incident power}} \tag{30}$$

which should be equal to unity for energy conservation. Thus we have also checked energy conservation to make sure that our results are physically correct.

We use the following methods to calculate the ocean emissivity and compare their accuracies: i) IBC; ii) MoM pulse/point matching; iii) MoM pulse/point matching + NIBC; iv) MoM Nystrom; v) MoM Nystrom + NIBC.

In Table 6, Table 7 and Table 8, the emissivities and the corresponding energy conservations from various methods are given. Table 6 shows the numerical results of emissivity obtained by IBC. The advantage of IBC is that there is only a single surface integral equation with only air green function g. This eliminates the use of dense grid. Thus only 10 points per wavelength is used. As shown in the table, energy conservation of IBC is satisfied to 50×10^{-4} for vertical polarization and 6.5×10^{-4} for horizontal polarization. Comparing to the Dual SIE results with dense grids shown in the following tables, IBC does not give accurate enough ocean emissivities, especially for vertical polarization.

Table 6. Emissivity and energy conservation given by IBC with different surface sampling densities.

Surface length is 60λ					
Number of Unknowns	Emissivity		Energy Conservation		Δx
	TM	TE	TM	TE	
600	0.394744	0.238267	0.994999	1.000647	$\frac{\lambda}{10}$

Table 7. Emissivity and energy conservation given by pulse/point matching and pulse/point matching + NIBC with different surface sampling densities.

Surface length is 60λ					
Number of Unknowns	Emissivity (with/without NIBC)		Energy Conservation (with/without NIBC)		Δx
	TM	TE	TM	TE	
3600	0.381721/0.381588	0.246651/0.246895	0.997049/0.997050	1.000271/1.000245	$\frac{\lambda}{30}$
7200	0.393640/0.393592	0.239148/0.239405	0.997487/0.997592	1.000077/1.000045	$\frac{\lambda}{60}$
14400	0.395614/0.395638	0.238299/0.238600	0.998235/0.998328	0.999977/0.999954	$\frac{\lambda}{120}$

In Table 7, the emissivities are given by MoM pulse/point matching with and without NIBC for different dense of profiles. For the emissivity of ocean surface with 120 points per wavelength density, the accuracies of these two methods are 19.74×10^{-4} and 20.46×10^{-4} for TM case, and 2.44×10^{-4} and 8.05×10^{-4} for TE case. Energy conservations for horizontal polarization are better than that for vertical polarization. Considering the Aquarius mission requirements, this means that MoM pulse/point matching on Dual SIE of 120 points per wavelength dense grid does not satisfy its accuracy requirements. For different dense samplings, the ocean surface emissivities calculated with pulse/point matching + NIBC have 3 decimal places of accuracy.

Table 8 shows the ocean emissivities and corresponding energy conservations obtained by MoM Nystrom with and without NIBC for different dense of profiles. The Nystrom method is described in Appendix A. The Nystrom uses 5th order basis function. Thus to have the same number of unknowns, here the surface sampling intervals are 5 times of those in pulse/point matching, i.e., $\Delta x = \frac{\lambda}{6}$, $\frac{\lambda}{12}$ and $\frac{\lambda}{24}$, respectively. Compared to pulse/point matching and IBC, Nystrom gives more accurate energy conservations on both vertical and horizontal polarizations for various surface sampling densities. For the emissivity of ocean surface with interval $\Delta x = \frac{\lambda}{24}$, namely, 240 surface unknowns per wavelength, the accuracies of MoM Nystrom are 1.845×10^{-4} for vertical polarization and 1.045×10^{-4} for horizontal polarization, respectively. These mean that MoM Nystrom with such dense discretization meets the accuracy requirement of Aquarius mission. In addition, in terms of NIBC, it has 6 decimal places of accuracy on emissivity and 8 decimal places of accuracy on energy conservation, which indicates NIBC with Nystrom can accelerate the calculation speed and also keep high accuracy on emissivity calculation.

Table 8. Emissivity and energy conservation given by Nystrom and Nystrom + NIBC with different surface sampling densities.

Surface length is 60λ					
Number of Unknowns	Emissivity (with/without NIBC)		Energy Conservation (with/without NIBC)		Δx
	TM	TE	TM	TE	
3600	0.39591010/0.39590992	0.23819768/0.23819780	0.99971876/0.99971876	0.99997406/0.99997406	$\frac{\lambda}{6}$
7200	0.39617730/0.39617724	0.23833828/0.23833832	0.99971938/0.99971938	0.99997417/0.99997417	$\frac{\lambda}{12}$
14400	0.39636175/0.39636171	0.23844277/0.23844279	0.99972281/0.99972281	0.99997432/0.99997432	$\frac{\lambda}{24}$

For the sake of intuitive comparison, the emissivities calculated by different methods for various dense grids are plotted in Figure 9. The error bars denote the differences of energy conservations and unit one for each. As shown in the figures, the method of MoM Nystrom + NIBC converges very well and has best energy conservations. This indicates that it has high accuracy of computing the ocean emissivity, which meets the accuracy requirement of Aquarius mission as demonstrated earlier. On the other hand, MoM pulse/point matching + NIBC converges relatively slow and doesn't give as high accuracy as MoM Nystrom + NIBC. The IBC gives worst energy conservations among three methods, which means its accuracy is lower than the other two methods.

5.2. Sensitivity of Emissivity to Salinity

One of NASA Aquarius mission objectives is to measure sea surface salinity (SSS) accurate to 0.2 psu. Since Nystrom + NIBC has high accuracy and fast speed on ocean emissivity calculation, we use this method to study the sensitivity of emissivity to sea surface salinity. In Figure 10, the ocean emissivities in two different realizations are shown in terms of sea surface salinity from 34 psu to 35 psu with 0.2 psu interval. These two different realizations correspond to two different ocean surface profiles. As the figures show, with the increasing of SSS, the emissivities of both horizontal and vertical polarizations decrease linearly. The changes of emissivities with the 0.2 psu SSS change are 4.9×10^{-4} for vertical polarization and 3.4×10^{-4} for the horizontal polarization. This result is consistent with previous

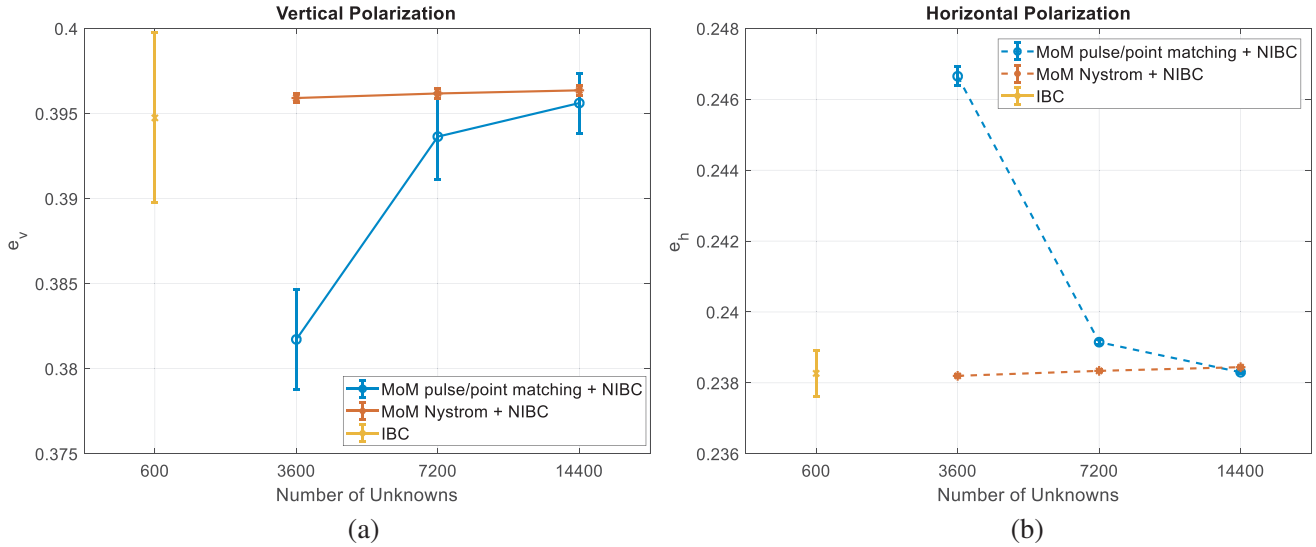

Figure 9. Comparison of emissivities calculated by IBC, MoM pulse/point matching + NIBC and MoM Nystrom + NIBC for different dense of profiles. The bars denote the differences of corresponding energy conservations and unit one. (a) Vertical polarization. (b) Horizontal polarization.

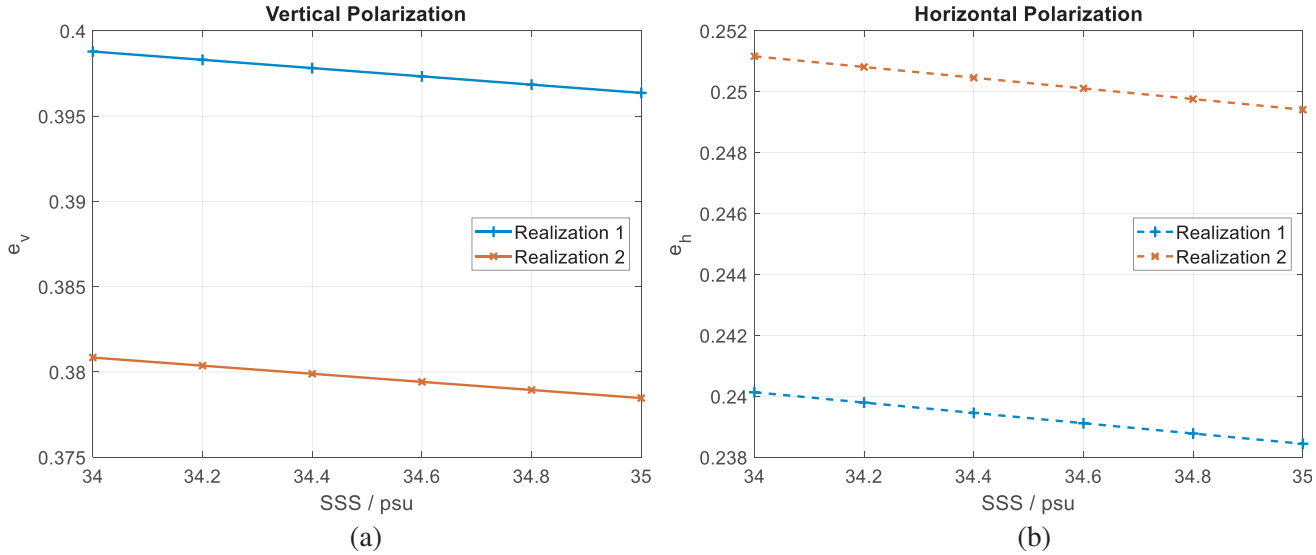

Figure 10. Emissivities calculated by Nystrom + NIBC in terms of sea surface salinity in two realizations. (a) Vertical polarization. (b) Horizontal polarization.

studies [16, 17]. In our two realizations, the differences of ocean emissivities are 1.8×10^{-2} for vertical polarization and 1.1×10^{-2} for the horizontal polarization, which are much larger the change due to salinity change. It is also noted that the curves of the two different realizations are parallel to each other, which means change of emissivity due to change of salinity is insensitive to different ocean surface geometries. This indicates that the Monte Carlo simulations can be applied in the numerical simulations for ocean emissivities utilizing our method. Although there are changes of emissivities due to realizations of ocean surfaces, the changes of emissivities due to salinity remain the same because the emissivities are calculated accurately for each realization.

6. CONCLUSIONS

In this paper, we have studied the electromagnetic scattering and emission from ocean surface by solving dual surface integral equations (Dual SIE) with numerical methods. However, when applying moment method on the Dual SIE to get accurate surface fields and emissivity, a dense discretization is required for two reasons: i) the much larger wavenumber of sea water due to its high permittivity; ii) fine scale feature of ocean surface geometry. A set of dense discretization will result in a large number of unknowns and expensive computational consumptions. What is more the dense grid will always bring up the slow convergence problems when the matrix equation is solved by iterative methods. To solve the Dual SIE efficiently, a neighborhood impedance boundary condition (NIBC) technique is proposed. In 2D problem, this method takes the impedance matrix as a banded matrix for the lower medium integral equation, and can dramatically reduce the cost of memory and CPU consumption. It also improves the property of impedance matrix so as to accelerate the convergence rate. The comparisons of surface fields and CPU time between NIBC and normal methods have shown that NIBC is both fast and accurate. We then use this method to calculate the ocean emissivity with MoM pulse/point matching and Nystrom method on the L-band. The sensitivity of emissivity to sea surface salinity is also investigated. Results show that, with the number of surface unknowns up to 240 per wavelength, emissivities calculated by using NIBC combined by MoM Nystrom are accurate to 2×10^{-4} for vertical polarization and 10^{-4} for the horizontal polarization. The proposed method is the first time that energy conservation is obeyed to 0.01%. Previous works were only within 0.5% [35, 36]. Such an accuracy meets the NASA Aquarius mission requirement to measure ocean salinity within 0.2 psu RMS [17]. In addition, through simulations using different profiles, we found that the changes of ocean emissivities due to SSS change are not influenced by the ocean geometry. The changes of emissivities due to salinity in the presence of ocean roughness remain a challenging problem in view of L-band missions of SMOS [37, 38], Aquarius [17–19], and the proposed MICAP [39]. There are also proposed space borne mission using P-band radiometers [40, 41].

Furthermore, the proposed NIBC in combination with Nystrom method should be rigorously pursued for 3D simulations. The NIBC method is using the band nature of the lower impedance matrices, which is based on physics. For the 3D case, NIBC will be a sparse matrix. We have not compared with results of analytic methods, as the purpose of this paper is to demonstrate energy conservation with the proposed new numerical method simulations of ocean scattering.

ACKNOWLEDGMENT

The high-performance computing facilities of FLUX at the University of Michigan, Ann Arbor, MI, USA, was used.

APPENDIX A.

The appendix presents the derivation of Nystrom method for the Dual SIE shown in Equations (1) and (2) [29, 30]. For the convenience of derivation, we change the independent variable from x to t.

For each interval, the 5 basis functions are 0th up to 4th order Legendre polynomials, which are listed as

$$\begin{aligned} F_1 &= P_0 = 1 \\ F_2 &= P_1 = t \\ F_3 &= P_2 = \frac{1}{2}\left(3t^2 - 1\right) \\ F_4 &= P_3 = \frac{1}{2}\left(5t^3 - 3t\right) \\ F_5 &= P_4 = \frac{1}{8}\left(35t^4 - 30t^2 + 3\right) \end{aligned} \tag{A1}$$

Thus to have a fair comparison with pulse basis functions, the interval Δx is 5 times larger.

Thus the surface integral equations are rewritten as

$$\frac{1}{2}\psi(t)+\int_{S_{pv}}dt'\left[K_N(t,t')\psi(t')\right]+\int_S dt'\left[K_D(t,t')u(t')\right]=\psi_{inc}(x(t),z(t)) \tag{A2}$$

$$-\frac{1}{2}\psi(t)+\int_{S_{pv}}dt'\left[K_{1N}(t,t')\psi(t')\right]+\int_S dt'\left[\frac{1}{\rho}K_{1D}(t,t')u(t')\right]=0 \tag{A3}$$

$$u(t')=\sqrt{1+(f'(x(t')))^2}\,\widehat{n}\cdot\nabla'\psi(t') \tag{A4}$$

where

$$\begin{aligned}
K_D(t,t') &= g(x(t),z(t);x(t'),z(t'))\\
K_{1D}(t,t') &= g_1(x(t),z(t);x(t'),z(t'))\\
K_N(t,t') &= -\sqrt{1+(f'(x(t')))^2}\left[\widehat{n}\cdot\nabla' g(x(t),z(t);x(t'),z(t'))\right]\\
K_{1N}(t,t') &= -\sqrt{1+(f'(x(t')))^2}\left[\widehat{n}\cdot\nabla' g_1(x(t),z(t);x(t'),z(t'))\right]
\end{aligned} \tag{A5}$$

Here the Green's functions for upper and lower medium are defined as

$$\begin{aligned}
g(t,t') &= \frac{i}{4}H_0^{(1)}\left(k\sqrt{[x(t)-x(t')]^2+[z(t)-z(t')]^2}\right)\\
g_1(t,t') &= \frac{i}{4}H_0^{(1)}\left(k_1\sqrt{[x(t)-x(t')]^2+[z(t)-z(t')]^2}\right)
\end{aligned} \tag{A6}$$

By applying moment method, we divide the rough surface into N_p patches. The unknown is approximated over each patch by a basis function expansion. For example, for each patch we use the

$$\psi(t')=\sum_{k=1}^{N_k}b_{k_p}^{\psi}F_k\left(t'_{local}\right) \tag{A7}$$

Note that p is the patch index, and t'_{local} is the local coordinate in that patch. Every patch has $k=1,\ldots,N_k$ basis functions. In our works, we use the 5th order Nystrom method, i.e., $N_k=5$.

Then the integration is done by quadrature rule

$$\int_{-1}^{1}f(t)\,dt=\sum_{i=1}^{n}w_i f(t_i) \tag{A8}$$

where

$$\begin{aligned}
t_i &= i\text{th zero for } P_n(t)\\
w_i &= \frac{2}{\left(1-t_i^2\right)\left(P_n'(t_i)\right)^2}
\end{aligned} \tag{A9}$$

Thus, the number of surface field unknowns is N_kN_p, and we have

$$\psi(\overline{r}')=\sum_{p=1}^{N_p}\sum_{k=1}^{N_k}b_{k_p}^{\psi}F_k(\overline{r}') \tag{A10}$$

We need to do an integral over the pth patch with the kernel

$$\psi_{inc}(\overline{r})=\int_S K(\overline{r},\overline{r}')\psi(\overline{r}')\,ds' \tag{A11}$$

Since there are N_k basis functions per patch, we also need to have N_k testing functions per patch. A set of smooth testing functions $T_l(\bar{r}')$ with support over each patch and complete to order N_k is introduced. Testing is on the mth patch

$$\begin{aligned} \int_{S_m} d\overline{r} T_l\left(\overline{r}\right)\psi_{inc}\left(\overline{r}\right) &= \int_{S_m} d\overline{r} T_l\left(\overline{r}\right)\sum_{p=1}^{N}\sum_{k=1}^{N_k} b_{k_p}^{\psi}\int_{S_p} K\left(\overline{r},\overline{r}'\right)F_k\left(\overline{r}'\right)ds' \\ m &= 1,2,...,N \\ l &= 1,2,...,N_k \end{aligned} \tag{A12}$$

$$\begin{aligned} \sum_{q=1}^{N_k} w_q T_l\left(\overline{r}_{q_m}\right)\psi_{inc}\left(\overline{r}_{q_m}\right) &= \sum_{q=1}^{N_k} w_q T_l\left(\overline{r}_{q_m}\right)\sum_{p=1}^{N}\sum_{k=1}^{N_k} b_{k_p}^{\psi}\int_{S_p} K\left(\overline{r}_{q_m},\overline{r}'\right)F_k\left(\overline{r}'\right)ds' \\ m &= 1,2,...,N \\ l &= 1,2,...,N_k \end{aligned} \tag{A13}$$

We define

$$\begin{aligned} Q_{lq} &= w_q T_l\left(\overline{r}_{q_m}\right) \\ q &= 1,2,...,N_k \\ l &= 1,2,...,N_k \end{aligned} \tag{A14}$$

$$\sum_{p=1}^{N}\sum_{k=1}^{N_k} b_{k_p}^{\psi}\int_{S_p} K\left(\overline{r}_{q_m},\overline{r}'\right)F_k\left(\overline{r}'\right)ds' = r_q \tag{A15}$$

Q is a $N_k \times N_k$ matrix, then

$$\sum_{q=1}^{N_k} Q_{lq}\psi_{inc}\left(\overline{r}_{q_m}\right) = \sum_{q=1}^{N_k} Q_{lq} r_q \tag{A16}$$

Since m is fixed on the mth patch, and Q_{lq} is a square matrix, we can take an inverse. Then we have

$$\begin{aligned} \overline{\overline{Q}\psi}_{inc} &= \overline{\overline{Q}}\overline{r} \\ \overline{\psi}_{inc} &= \overline{r} \end{aligned} \tag{A17}$$

$$\begin{aligned} \psi_{inc}\left(\overline{r}_{q_m}\right) &= \sum_{p=1}^{N}\sum_{k=1}^{N_k} b_{k_p}^{\psi}\int_{S_p} K\left(\overline{r}_{q_m},\overline{r}'\right)F_k\left(\overline{r}'\right)ds' \\ q &= 1,2,...,N_k \\ m &= 1,2,...,N \end{aligned} \tag{A18}$$

For each m, p is split into near and far field shown as

$$\psi_{inc}\left(\overline{r}_{q_m}\right) = \sum_{p\in far_m}\sum_{k=1}^{N_k} b_{k_p}^{\psi}\int_{S_p} K\left(\overline{r}_{q_m},\overline{r}'\right)F_k\left(\overline{r}'\right)ds' + \sum_{p\in near_m}\sum_{k=1}^{N_k} b_{k_p}^{\psi}\int_{S_p} K\left(\overline{r}_{qm},\overline{r}'\right)F_k\left(\overline{r}'\right)ds' \tag{A19}$$

For far field, we map $\bar{r}'$ into t' and then map locally to t'_{local}, then

$$\begin{aligned} t' &= \frac{\Delta t}{2}t'_{\text{local}} + \left(t'_{\text{beg}} + \frac{\Delta t}{2}\right) \\ \Delta t &= t'_{\text{end}} - t'_{\text{beg}} \\ -1 &\le t'_{\text{local}} \le 1 \end{aligned} \tag{A20}$$

$$\int_{S_p} K\left(\overline{r}_{q_m},\overline{r}'\right) F_k\left(\overline{r}'\right)ds' = \frac{\Delta t}{2}\sum_{q_p=1}^{N_k} w_q K\left(\overline{r}_{q_m},\overline{r}_{q_p}\right) F_k\left(\overline{r}_{q_p}\right)$$
$$ds' = dt' = \frac{\Delta t}{2} dt'_{local} \tag{A21}$$

$\bar{r}_{q_p}$ is the location of points according to the zeros of P_{N_k}. Then we have

$$\begin{aligned}\psi_{inc}\left(\overline{r}_{q_m}\right) = &\sum_{p\in near_m}\sum_{k=1}^{N_k} b_{k_p}^{\psi}\int_{S_p} K\left(\overline{r}_{q_m},\overline{r}'\right) F_k\left(\overline{r}'\right)ds' \\ &+ \sum_{p\in far_m}\sum_{k=1}^{N_k} b_{k_p}^{\psi}\frac{\Delta t}{2}\sum_{q_p=1}^{N_k} w_q K\left(\overline{r}_{q_m},\overline{r}_{q_p}\right) F_k\left(\overline{r}_{q_p}\right) \\ q &= 1,2,...,N_k \\ m &= 1,2,...,N\end{aligned} \tag{A22}$$

However, since

$$\psi_p\left(\overline{r}_{q_p}\right) = \sum_{k=1}^{N_k} b_{k_p}^{\psi} F_k\left(\overline{r}_{q_p}\right) \tag{A23}$$

We have

$$\begin{aligned}\psi_{inc}\left(\overline{r}_{q_m}\right) = &\sum_{p\in near_m}\sum_{k=1}^{N_k} b_{k_p}^{\psi}\int_{S_p} K\left(\overline{r}_{q_m},\overline{r}'\right) F_k\left(\overline{r}'\right)ds' + \sum_{p\in far_m}\sum_{q_p=1}^{N_k}\frac{\Delta t}{2} w_q K\left(\overline{r}_{q_m},\overline{r}_{q_p}\right)\psi_p\left(\overline{r}_{q_p}\right) \\ q_m &= 1,2,...,N_k \\ m &= 1,2,...,N \\ p &= 1,2,...,N\end{aligned} \tag{A24}$$

For near field, $\int_{S_p} K\left(\overline{r}_{qm},\overline{r}'\right) F_k\left(\overline{r}'\right)ds'$ has singular integrand for self patch so that we need quadrature to handle this singularity. Let

$$\int_{S_p} K\left(\overline{r}_{q_m},\overline{r}'\right) F_k\left(\overline{r}'\right)ds' = \sum_{j=1}^{N_k} w_j^{q_m} F_k\left(\overline{r}_{j_p}\right)$$
$$k = 1,2,...,N_k \tag{A25}$$

Then we have

$$\begin{bmatrix} F_1\left(\overline{r}_{1_p}\right) & F_1\left(\overline{r}_{2_p}\right) & F_1\left(\overline{r}_{3_p}\right) & F_1\left(\overline{r}_{4_p}\right) & F_1\left(\overline{r}_{5_p}\right) \\ F_2\left(\overline{r}_{1_p}\right) & F_2\left(\overline{r}_{2_p}\right) & F_2\left(\overline{r}_{3_p}\right) & F_2\left(\overline{r}_{4_p}\right) & F_2\left(\overline{r}_{5_p}\right) \\ F_3\left(\overline{r}_{1_p}\right) & F_3\left(\overline{r}_{2_p}\right) & F_3\left(\overline{r}_{3_p}\right) & F_3\left(\overline{r}_{4_p}\right) & F_3\left(\overline{r}_{5_p}\right) \\ F_4\left(\overline{r}_{1_p}\right) & F_4\left(\overline{r}_{2_p}\right) & F_4\left(\overline{r}_{3_p}\right) & F_4\left(\overline{r}_{4_p}\right) & F_4\left(\overline{r}_{5_p}\right) \\ F_5\left(\overline{r}_{1_p}\right) & F_5\left(\overline{r}_{2_p}\right) & F_5\left(\overline{r}_{3_p}\right) & F_5\left(\overline{r}_{4_p}\right) & F_5\left(\overline{r}_{5_p}\right) \end{bmatrix} \begin{bmatrix} w_1^{q_m} \\ w_2^{q_m} \\ w_3^{q_m} \\ w_4^{q_m} \\ w_5^{q_m} \end{bmatrix} = \begin{bmatrix} \int_{S_p} K\left(\overline{r}_{qm},\overline{r}'\right) F_1\left(\overline{r}'\right)ds' \\ \int_{S_p} K\left(\overline{r}_{qm},\overline{r}'\right) F_2\left(\overline{r}'\right)ds' \\ \int_{S_p} K\left(\overline{r}_{qm},\overline{r}'\right) F_3\left(\overline{r}'\right)ds' \\ \int_{S_p} K\left(\overline{r}_{qm},\overline{r}'\right) F_4\left(\overline{r}'\right)ds' \\ \int_{S_p} K\left(\overline{r}_{qm},\overline{r}'\right) F_5\left(\overline{r}'\right)ds' \end{bmatrix} \tag{A26}$$

Note the rows are the basis functions P_0, P_1, P_2, P_3, P_4, then

$$\psi_{inc}\left(\overline{r}_{q_m}\right) = \sum_{p\in near_m}\sum_{k=1}^{N_k} b_{k_p}^{\psi}\sum_{j=1}^{N_k} w_{j_p}^{q_m} F_k\left(\overline{r}_{j_p}\right) + \sum_{p\in far_m}\sum_{q_p=1}^{N_k}\frac{\Delta t}{2} w_q K\left(\overline{r}_{q_m},\overline{r}_{q_p}\right)\psi_p\left(\overline{r}_{q_p}\right) \tag{A27}$$

On the pth patch,

$$\psi\left(\overline{r}'\right) = \psi\left(t'\right) = \sum_{k=1}^{N_k} b_{k_p}^{\psi} F_k\left(t'_{\text{local}}\right)$$
$$u\left(\overline{r}'\right) = u\left(t'\right) = \sum_{k=1}^{N_k} b_{k_p}^{u} F_k\left(t'_{\text{local}}\right) \tag{A28}$$

where w_q is the weight of Gauss Legendre quadrature taken for $-1 \leq t_{\text{local}} \leq 1$.

Now considering the surface integral equation for dielectric rough surface shown in Equation (A1), we use the Nystrom method and have

$$\begin{aligned}
\psi_{inc}\left(\overline{r}_{q_m}\right) = & \frac{1}{2}\psi\left(\overline{r}_{q_m}\right) + \sum_{p\in\text{near}}\sum_{k=1}^{N_k} b_{k_p}^{\psi}\int_{S_p} K_N\left(\overline{r}_{q_m},\overline{r}'\right)F_k\left(\overline{r}'\right)ds' \\
& + \sum_{p\in\text{far}}\sum_{q_p=1}^{N_k} b_{k_p}^{\psi}\frac{\Delta t}{2}\sum_{q_p=1}^{N_k} w_q K\left(\overline{r}_{q_m},\overline{r}_{q_p}\right)F_k\left(\overline{r}_{q_p}\right) \\
& + \sum_{p\in near}\sum_{k=1}^{N_k} b_{k_p}^{u}\int_{S_p} K_D\left(\overline{r}_{q_m},\overline{r}'\right)F_k\left(\overline{r}'\right)ds' \\
& + \sum_{q_p=1}^{N_k} b_{k_p}^{u}\frac{\Delta t}{2}\sum_{q_p=1}^{N_k} w_q K\left(\overline{r}_{q_m},\overline{r}_{q_p}\right)F_k\left(\overline{r}_{q_p}\right) \\
q = & 1,2,...,N_k \\
m = & 1,2,...,N
\end{aligned} \tag{A29}$$

$$\begin{aligned}
\psi_{inc}\left(\overline{r}_{q_m}\right) = & \frac{1}{2}\psi\left(\overline{r}_{q_m}\right) + \sum_{p\in\text{near}}\sum_{k=1}^{N_k} b_{k_p}^{\psi}\int_{S_p} K_N\left(\overline{r}_{q_m},\overline{r}'\right)F_k\left(\overline{r}'\right)ds' \\
& + \sum_{p\in\text{far}}\sum_{q_p=1}^{N_k}\frac{\Delta t}{2} w_q K_N\left(\overline{r}_{q_m},\overline{r}_{q_p}\right)\psi_p\left(\overline{r}_{q_p}\right) \\
& + \sum_{p\in near}\sum_{k=1}^{N_k} b_{k_p}^{u}\int_{S_p} K_D\left(\overline{r}_{q_m},\overline{r}'\right)F_k\left(\overline{r}'\right)ds' \\
& + \sum_{p\in far}\sum_{q_p=1}^{N_k}\frac{\Delta t}{2} w_q K_D\left(\overline{r}_{q_m},\overline{r}_{q_p}\right)u_p\left(\overline{r}_{q_p}\right) \\
q = & 1,2,...,N_k \\
m = & 1,2,...,N
\end{aligned} \tag{A30}$$

Then

$$\begin{aligned}
\psi_{inc}\left(\overline{r}_{q_m}\right) = & \frac{1}{2}\psi\left(\overline{r}_{q_m}\right) + \sum_{p\in near}\sum_{k=1}^{N_k} b_{k_p}^{\psi}\sum_{j=1}^{N_k} w_j^{(N)} F_k\left(\overline{r}_{j_p}\right) \\
& + \sum_{p\in far}\sum_{q_p=1}^{N_k}\frac{\Delta t}{2} w_q K_N\left(\overline{r}_{q_m},\overline{r}_{q_p}\right)\psi_p\left(\overline{r}_{q_p}\right) \\
& + \sum_{p\in near}\sum_{k=1}^{N_k} b_{k_p}^{u}\sum_{j=1}^{N_k} w_j^{(D)} F_k\left(\overline{r}_{j_p}\right) + \sum_{p\in far}\sum_{q_p=1}^{N_k}\frac{\Delta t}{2} w_q K_D\left(\overline{r}_{q_m},\overline{r}_{q_p}\right)u_p\left(\overline{r}_{q_p}\right) \\
j,q = & 1,2,...,N_k \\
m = & 1,2,...,N
\end{aligned} \tag{A31}$$

$$\begin{aligned}\psi_{inc}\left(\overline{r}_{q_m}\right) = & \frac{1}{2}\psi\left(\overline{r}_{q_m}\right) + \sum_{p\in near}\sum_{k=1}^{N_k} w_j^{(N)}\psi_p\left(\overline{r}_{j_p}\right) \\ & + \sum_{p\in far}\sum_{q_p=1}^{N_k}\frac{\Delta t}{2}w_q K_N\left(\overline{r}_{q_m},\overline{r}_{q_p}\right)\psi_p\left(\overline{r}_{q_p}\right) \\ & + \sum_{p\in near}\sum_{k=1}^{N_k} w_j^{(D)}u_p\left(\overline{r}_{j_p}\right) + \sum_{p\in far}\sum_{q_p=1}^{N_k}\frac{\Delta t}{2}w_q K_D\left(\overline{r}_{q_m},\overline{r}_{q_p}\right)u_p\left(\overline{r}_{q_p}\right) \\ & j,q = 1,2,...,N_k \\ & m = 1,2,...,N\end{aligned} \tag{A32}$$

Note that the summation over q and j is over the quadrature points, and the summation over k is over the basis functions.

Similarly, for the surface integral equation for lower medium, we have

$$\begin{aligned}& -\frac{1}{2}\psi\left(\overline{r}_{q_m}\right) + \sum_{p\in near}\sum_{k=1}^{N_k} w_j^{(1N)}\psi_p\left(\overline{r}_{j_p}\right) + \sum_{p\in far}\sum_{q_p=1}^{N_k}\frac{\Delta t}{2}w_q K_{1N}\left(\overline{r}_{q_m},\overline{r}_{q_p}\right)\psi_p\left(\overline{r}_{q_p}\right) \\ & + \frac{1}{\rho}\sum_{p\in \text{near}}\sum_{k=1}^{N_k} w_j^{(1D)}u_p\left(\overline{r}_{j_p}\right) + \frac{1}{\rho}\sum_{p\in \text{far}}\sum_{q_p=1}^{N_k}\frac{\Delta t}{2}w_q K_{1D}\left(\overline{r}_{q_m},\overline{r}_{q_p}\right)u_p\left(\overline{r}_{q_p}\right) = 0 \\ & j,q = 1,2,...,N_k \\ & m = 1,2,...,N\end{aligned} \tag{A33}$$

To implement our NIBC with Nystrom, we set $K_{1N}\left(\overline{r}_{q_m},\overline{r}_{q_p}\right)$ and $K_{1D}\left(\overline{r}_{q_m},\overline{r}_{q_p}\right)$ equal to zero when the distances between source points and field points are larger than BW.

REFERENCES

1. Ulaby, F. T. and D. G. Long, *Microwave Radar and Radiometric Remote Sensing*, University of Michigan Press, Ann Arbor, 2015.
2. Fung, A. K. and K. S. Chen, *Microwave Scattering and Emission Models for Users*, Artech House, 2010.
3. Tsang, L., J. A. Kong, and R. T. Shin, *Theory of Microwave Remote Sensing*, Wiley, New York, 1985.
4. Yueh, S., R. Kwok, F. Li, S. Nghiem, and W. Wilson, "Polarimetric passive remote sensing of ocean wind vectors," *Radio Science*, Vol. 29, No. 4, 799–814, Jul. 1994.
5. Irisov, V. G., "Small-slope expansion for thermal and reflected radiation from a rough surface," *Waves in Random Media*, Vol. 7, 1–10, Jan. 1997.
6. Gu, X. X., L. Tsang, H. Braunisch, and P. Xu, "Modeling absorption of rough interface between dielectric and conductive medium," *Microwave and Optical Technology Letters*, Vol. 49, 7–13, Jan. 2007.
7. Chen, K. S., T. D. Wu, L. Tsang, Q. Li, J. C. Shi, and A. K. Fung, "Emission of rough surfaces calculated by the integral equation method with comparison to three-dimensional moment method simulations," *IEEE Transactions on Geoscience and Remote Sensing*, Vol. 41, 90–101, Jan. 2003.
8. Johnson, J. T., "A study of ocean-like surface thermal emission and reflection using Voronovich's small slope approximation," *IEEE Transactions on Geoscience and Remote Sensing*, Vol. 43, 306–314, Feb. 2005.
9. Guerin, C. A. and J. T. Johnson, "A simplified formulation for rough surface cross-polarized backscattering under the second-order small-slope approximation," *IEEE Transactions on Geoscience and Remote Sensing*, Vol. 53, 6308–6314, Nov. 2015.

10. Voronovich, A., "Small-slope approximation for electromagnetic-wave scattering at a rough interface of dielectric half-spaces," *Waves in Random Media*, Vol. 4, 337–367, Jul. 1994.
11. Johnson, J. and M. Zhang, "Theoretical study of the small slope approximation for ocean polarimetric thermal emission," *IEEE Transactions on Geoscience and Remote Sensing*, Vol. 37, No. 5, 2305–2316, Sep. 1999.
12. Irisov, V., "Small-slope expansion for thermal and reflected radiation from a rough surface," *Waves in Random Media*, Vol. 7, No. 1, 1–10, Jan. 1997.
13. Plant, W. J., "A two-scale model of short wind-generated waves and scatterometry," *Journal of Geophysical Research: Oceans*, Vol. 91, No. C9, 10735–10749, 1986.
14. Johnson, J. T., "An efficient two-scale model for the computation of thermal emission and atmospheric reflection from the sea surface," *IEEE Transactions on Geoscience and Remote Sensing*, Vol. 44, 560–568, Mar. 2006.
15. Yueh, S., "Modeling of wind direction signals in polarimetric sea surface brightness temperatures," *IEEE Transactions on Geoscience and Remote Sensing*, Vol. 35, No. 6, 1400–1418, Nov. 1997.
16. Lagerloef, G., F. R. Colomb, D. Le Vine, F. Wentz, S. Yueh, C. Ruf, et al., "The aquarius/SAC-D mission: Designed to meet the salinity remote-sensing challenge," *Oceanography*, Vol. 21, 68–81, Mar. 2008.
17. Le Vine, D. M., E. P. Dinnat, T. Meissner, S. H. Yueh, F. J. Wentz, S. E. Torrusio, et al., "Status of aquarius/SAC-D and aquarius salinity retrievals," *IEEE Journal of Selected Topics in Applied Earth Observations and Remote Sensing*, Vol. 8, 5401–5415, Dec. 2015.
18. Fore, A. G., S. H. Yueh, W. Q. Tang, B. W. Stiles, and A. K. Hayashi, "Combined active/passive retrievals of ocean vector wind and sea surface salinity with SMAP," *IEEE Transactions on Geoscience and Remote Sensing*, Vol. 54, 7396–7404, Dec. 2016.
19. Yueh, S., W. Q. Tang, A. Fore, A. Hayashi, Y. T. Song, and G. Lagerloef, "Aquarius geophysical model function and combined active passive algorithm for ocean surface salinity and wind retrieval," *Journal of Geophysical Research-Oceans*, Vol. 119, 5360–5379, Aug. 2014.
20. Yang, J. S., Y. Du, and J. C. Shi, "Polarimetric simulations of bistatic scattering from perfectly conducting ocean surfaces with 3 m/s wind speed at L-band," *IEEE Journal of Selected Topics in Applied Earth Observations and Remote Sensing*, Vol. 9, 1176–1186, Mar. 2016.
21. Johnson, J. T., R. T. Shin, J. A. Kong, L. Tsang, and K. Pak, "A numerical study of ocean polarimetric thermal emission," *IEEE Transactions on Geoscience and Remote Sensing*, Vol. 37, 8–20, Jan. 1999.
22. Ao, C. O., P. O. Orondo, Y. Zhang, and J. A. Kong, "Electromagnetic model of thermal emission from foam-covered ocean surface using dense medium radiative transfer theory," *IGARSS 2000: IEEE 2000 International Geoscience and Remote Sensing Symposium, Vol. I–VI, Proceedings*, 1277–1279, 2000.
23. Soriano, G., C. A. Guerin, and M. Saillard, "Microwave ocean scattering at low-grazing angles with the GMoM," *7th European Radar Conference*, 5–8, 2010.
24. Johnson, J. T. and H. T. Chou, "Numerical studies of low grazing angle backscatter from 1D and 2D impedance surfaces," *1998 IEEE International Geoscience and Remote Sensing Symposium (IGARSS)*, Vol. 4, 2295–2297, 1998.
25. Qiao, T., L. Tsang, D. Vandemark, S. Yueh, T. H. Liao, F. Nouguier, and B. Chapron, "Sea surface radar scattering at L-band based on numerical solution of Maxwell's equations in 3-D (NMM3D)," *IEEE Transactions on Geoscience and Remote Sensing*, Vol. 56, No. 6, 3137–3147, Jun. 2018.
26. Tsang, L., J. A. Kong, and R. T. Shin, *Scattering of Electromagnetic Waves, Vol. 2, Scattering of Electromagnetic Waves: Numerical Simulations*, John Wiley & Sons, 2000.
27. Toporkov, J., R. Marchand, and G. Brown, "On the discretization of the integral equation describing scattering by rough conducting surfaces," *IEEE Transactions on Antennas and Propagation*, Vol. 46, No. 1, 150–161, Jan. 1998.

28. Tsang, L. and Q. Li, "Numerical solution of scattering of waves by lossy dielectric surfaces using a physics-based two-grid method," *Microwave and Optical Technology Letters*, Vol. 16, 356–364, Dec. 20, 1997.
29. Canino, L. F., J. J. Ottusch, M. A. Stalzer, J. L. Visher, and S. M. Wandzura, "Numerical solution of the Helmholtz equation in 2D and 3D using a high-order Nystrom discretization," *Journal of Computational Physics*, Vol. 146, 627–663, Nov. 1, 1998.
30. Gedney, S. D., "On deriving a locally corrected Nystrom scheme from a quadrature sampled moment method," *IEEE Transactions on Antennas and Propagation*, Vol. 51, 2402–2412, Sep. 2003.
31. Elfouhaily, T., B. Chapron, K. Katsaros, and D. Vandemark, "A unified directional spectrum for long and short wind-driven waves," *Journal of Geophysical Research-Oceans*, Vol. 102, 15781–15796, Jul. 15, 1997.
32. Qiao, T., L. Tsang, and S. Tan, "Scattering of lossy dielectric surfaces in full wave simulation of Maxwell's equations with dense grid and neighborhood impedance boundary conditions," *2017 Progress In Electromagnetics Research Symposium — Fall (PIERS — FALL)*, 3054–3057, Singapore, Nov. 19–22, 2017.
33. Klein, L. A. and C. T. Swift, "Improved model for dielectric-constant of sea-water at microwave-frequencies," *IEEE Transactions on Antennas and Propagation*, Vol. 25, 104–111, 1977.
34. Liao, T. H., L. Tsang, S. W. Huang, N. Niamsuwan, S. Jaruwatanadilok, S. B. Kim, et al., "Copolarized and cross-polarized backscattering from random rough soil surfaces from L-band to Ku-band using numerical solutions of Maxwell's equations with near-field precondition," *IEEE Transactions on Geoscience and Remote Sensing*, Vol. 54, 651–662, Feb. 2016.
35. Tsang, L., I. S. Koh, T. H. Liao, S. W. Huang, X. L. Xu, E. G. Njoku, et al., "Active and passive vegetated surface models with rough surface boundary conditions from NMM3D," *IEEE Journal of Selected Topics in Applied Earth Observations and Remote Sensing*, Vol. 6, 1698–1709, Jun. 2013.
36. Huang, S. W., L. Tsang, E. G. Njoku, and K. S. Chan, "Backscattering coefficients, coherent reflectivities, and emissivities of randomly rough soil surfaces at L-band for SMAP applications based on numerical solutions of maxwell equations in three-dimensional simulations," *IEEE Transactions on Geoscience and Remote Sensing*, Vol. 48, 2557–2568, Jun. 2010.
37. Camps, A., N. Vall-llossera, N. Duffo, F. Torres, and I. Corbella, "Performance of sea surface salinity and soil moisture retrieval algorithms with different auxiliary datasets in 2-D L-band aperture synthesis interferometric radiometers," *IEEE Transactions on Geoscience and Remote Sensing*, Vol. 43, 1189–1200, May 2005.
38. Camps, A., J. Font, M. Vall-Llossera, I. Corbella, N. Duffo, F. Torres, et al., "Determination of the sea surface emissivity at L-band and application to SMOS salinity retrieval algorithms: Review of the contributions of the UPC-ICM," *Radio Science*, Vol. 43, Jun. 20, 2008.
39. Zhang, C., H. Liu, L. Wu, and J. Wu, "Imaging simulation of the microwave radiometer aboard the micap for sea surface salinity measurement," *2015 IEEE International Geoscience and Remote Sensing Symposium (IGARSS)*, 3469–3472, 2015.
40. Misra, S., S. Brow, S. Yueh, and T. Lee, "Enabling the next generation of salinity, sea surface temperature and wind measurements from space: Instrument challenges," *Progress In Electromagnetics Research Symposium Abstracts*, 319, Singapore, Nov. 19–22, 2017.
41. Brow, S., S. Misra, S. Yueh, and T. Lee, "A next generation spaceborne ocean state observatory: Surface salinity, temperature and ocean winds from equator to Pole," *Progress In Electromagnetics Research Symposium Abstracts*, 320, Singapore, Nov. 19–22, 2017.